

**ECONOMIC GEOLOGY
RESEARCH UNIT**

University of the Witwatersrand
Johannesburg

— • —

**PYRITE-GOLD ASSOCIATION IN DOLOMITES
AND CARBONATED METAVOLCANICS FROM TURK
MINE, ZIMBABWE: AN INVESTIGATION LINKING
LATE SHEARING AND GOLD INTRODUCTION**

**E. XENOPHONTOS, G. STEVENS
and W.J. PRZYBYLOWICZ**

— • INFORMATION CIRCULAR No. 328

UNIVERSITY OF THE WITWATERSRAND
JOHANNESBURG

**PYRITE-GOLD ASSOCIATION IN DOLOMITES AND CARBONATED
METAVOLCANICS FROM TURK MINE, ZIMBABWE: AN INVESTIGATION
LINKING LATE SHEARING AND GOLD INTRODUCTION**

by

E. XENOPHONTOS^a, G. STEVENS^a and W.J. PRZYBYLOWICZ^b

*^a Economic Geology Research Unit, University of the Witwatersrand, Private Bag 3, PO
WITS, 2050, South Africa*

*^b Van de Graaff Group, National Accelerator Centre, PO Box 72, Faure 7131, South
Africa)*

**ECONOMIC GEOLOGY RESEARCH UNIT
INFORMATION CIRCULAR No. 328**

November, 1998

**PYRITE-GOLD ASSOCIATION IN DOLOMITES AND CARBONATED
METAVOLCANICS FROM TURK MINE, ZIMBABWE: AN INVESTIGATION
LINKING LATE SHEARING AND GOLD INTRODUCTION**

ABSTRACT

In this study, micro-PIXE analyses were used to study pyrite geochemistry as well as the gold-pyrite association in the vicinity of Turk Mine, Bubi greenstone belt, Zimbabwe. The sample material consisted of pyrites from two sites of known gold enrichment in this area of the belt i.e. from a pyrite-enriched carbonate sequence developed to the east of Turk Mine, and from the quartz + carbonate + pyrite altered metabasalt of the Turk Mine gold deposit. In the carbonate sequence, petrographic study revealed several generations of pyrite crystals: (1) pyrite introduced into breccia horizons as sedimentary clasts; (2) pyrite produced through pseudomorphic replacement of Fe-rich sedimentary structures within sedimentary breccia horizons; (3) poikiloblastic euhedral pyrite crystals; and (4) inclusion-free euhedral pyrite crystals. A single pyrite generation was identified in the metavolcanic samples, which correlates texturally with the inclusion-free euhedral pyrite in the carbonate sequence. Pyrite $\delta^{34}\text{S}$ values from the carbonate sequence rocks are interpreted to indicate a mixed source of sulphur. Most samples have $\delta^{34}\text{S}$ values close to 0 ‰, and this is interpreted to reflect a magmatic sulphur source. A small proportion of the samples had $\delta^{34}\text{S}$ values that ranged from 4 ‰ to 16 ‰. These values are interpreted to reflect a component of sulphur derived from sedimentary sulphate minerals. The samples with the highest $\delta^{34}\text{S}$ values contained a high proportion of the poikiloblastic euhedral pyrite (> 40 modal prop.). Elemental maps of all pyrite generations in both rock types were obtained using Dynamic Analysis (a rapid matrix transform method) which forms part of the GeoPIXE software package. These were complemented by point analyses in selected areas. The implemented on-demand beam deflection system allowed for count rates of the order of 3000 counts per second, with negligible dead time. The distribution of As and other elements confirmed the petrographic interpretation of several different pyrite generations in the carbonate sequence. Gold concentrations in the pyrites analysed from the carbonate sequence were too low for gold introduction to be positively correlated with a particular pyrite generation. However, in the altered metabasalts of the Turk ore deposit, gold introduction can be shown to be the product of fluid influx along late micro-shears. These micro-shears post-date the formation of the quartz-carbonate-pyrite alteration assemblage and were responsible for the brecciation of the original euhedral pyrite crystals. Thus, a two-stage alteration and mineralization model is indicated for this deposit.

_____oOo_____

**PYRITE-GOLD ASSOCIATION IN DOLOMITES AND CARBONATED
METAVOLCANICS FROM TURK MINE, ZIMBABWE: AN INVESTIGATION
LINKING LATE SHEARING AND GOLD INTRODUCTION**

CONTENTS

	Page
INTRODUCTION	1
GEOLOGICAL SETTING	1
Archaean Stratigraphy of Zimbabwe	1
Geology of the Turk Mine Area	2
BOREHOLE LITHOLOGICAL SEQUENCE	4
Carbonate Sequence	4
Turk Deposit	5
Pyrite-bearing Zones	5
PETROGRAPHY	7
Pyrite Textures in the Carbonate Sequence	7
<i>Pseudomorphic Pyrite</i>	7
<i>Pyrite Clasts</i>	8
<i>Euhedral Pyrite</i>	8
<i>Massive Pyrite</i>	8
Pyrite Textures in the Metavolcanics	9
SULPHUR ISOTOPE ANALYSES	10
Laboratory Technique	10
Sulphur Isotope Ratios and Results	11
PROTON INDUCED X-RAY EMISSION (PIXE) ANALYSES	13
Pyrite Geochemistry	14
Gold Introduction	16
DISCUSSION AND CONCLUSIONS	18
ACKNOWLEDGEMENTS	20
REFERENCES	20

_____oOo_____

Published by the Economic Geology Research Unit
Department of Geology
University of the Witwatersrand
1 Jan Smuts Avenue
Johannesburg 2001
South Africa

ISBN 1-86838-241-9

PYRITE-GOLD ASSOCIATION IN DOLOMITES AND CARBONATED METAVOLCANICS FROM TURK MINE, ZIMBABWE: AN INVESTIGATION LINKING LATE SHEARING AND GOLD INTRODUCTION

INTRODUCTION

The Turk Mine in the Bubi greenstone belt is situated to the northeast of Bulawayo, Zimbabwe (Fig 1). This area has been the focus of gold mining and exploration activity since 1921. The main ore body mined at Turk occurs within sheared metabasalts. The shearing of the metabasalts has resulted in fluid introduction, the precipitation of quartz veins, widespread carbonate alteration of the metabasalts and gold introduction into specific zones. Thus, the current focus of mining is an epithermal shear zone hosted lode gold deposit similar to many of the other gold mines and deposits that occur in the Bubi greenstone belt. In addition to the known Turk deposit, preliminary geochemical observations by exploration geologists of CASMYN Mining, who are currently developing Turk Mine and conducting gold exploration in the general area, have revealed significant gold grades in oxidized gossanous material derived from pyrite-rich zones developed along the contact between the metabasalts and a carbonate sequence approximately 500m to the east of Turk Mine. At the time of this study, two boreholes had been drilled through this sequence exposing approximately 150 m of the carbonate sequence in each hole. In both cases, the carbonate sediments contain complex pyrite populations that occur in both sheared and unsheared settings. This pyrite mineralization, as well as that developed within the Turk Mine ore is the focus of this study. The aim of this project has been to document the geochemistry of the pyrite populations in the sediments and in the metabasalt ore as well as to investigate the gold-pyrite association in both rock types.

GEOLOGICAL SETTING

Archaeon Stratigraphy of Zimbabwe

The Zimbabwe Craton underlies approximately seventy per cent of the country and is bounded to the south by the Limpopo Belt, and to the east and to the north by the late Precambrian Mozambique and Zambezi Belts respectively. The western margin of the Craton is situated in the eastern part of Botswana and is overlain by Proterozoic and Mesozoic cover. Within the Zimbabwean Craton, the greenstone stratigraphy has been divided into three greenstone groups. The oldest and lowermost Sebakwian Group consists of variably metamorphosed volcano-sedimentary rocks, including banded iron formations and mafic to ultramafic rocks. The Bulawayan Group overlies the Sebakwian; this is the most extensive of the supracrustal sequences. The Bulawayan Group is divided into a poorly exposed Lower Greenstone Group dominated by mafic lavas, and a well-preserved Upper Greenstone unit consisting of mafic lavas and intermediate agglomerates (Condie, 1981).

The Bulawayan Group is unconformably overlain by the volcano-sedimentary Shamvaian Group (Fig 1). Two suites of late granitoids intrude the Upper Greenstones and the Shamvaian Group rocks (Wilson, 1979). These include the Sesombi Suite of tonalites and the Chilimanzi Suite of adamellites. The final major magmatic event within the Craton was the intrusion of the Great Dyke at about 2.5 Ga (Wilson et al., 1978).

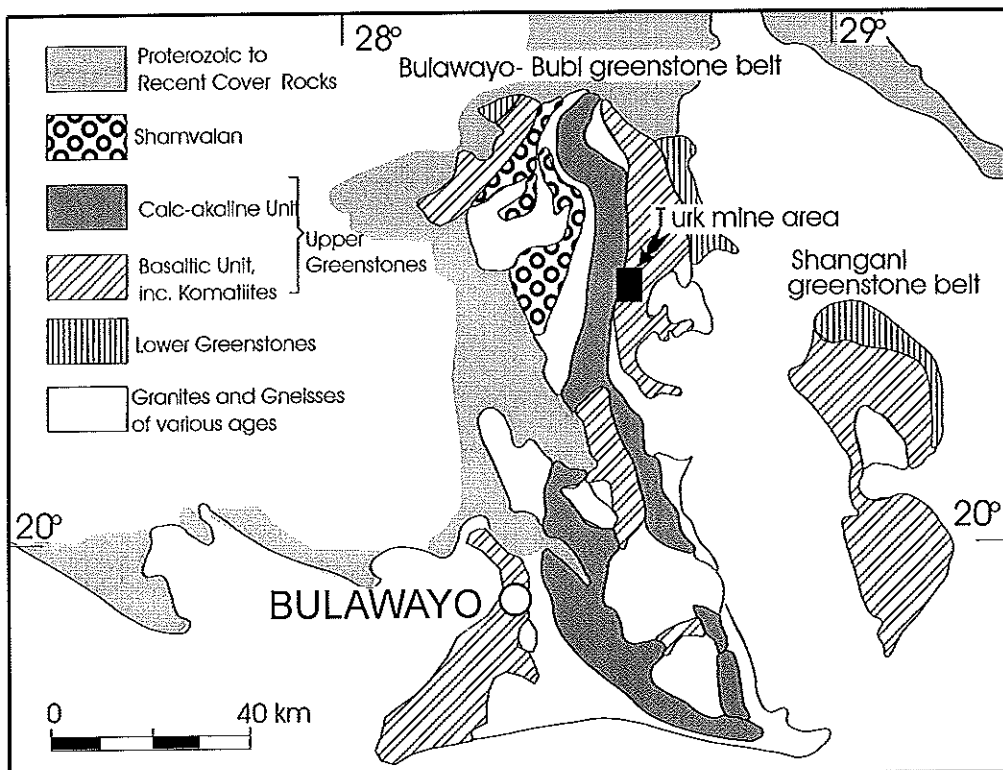


Figure 1: Regional geology of the Bulawayo-Bubi granite-greenstone terrane (modified after Amm, 1940; Macgregor et al., 1937; Wilson, 1979)

Geology of the Turk Mine Area

The rocks exposed in the Bubi greenstone belt in the area of Turk Mine (Fig. 2) are typical of the Upper Bulawayan Group, these rocks have an approximate age of 2.7 Ga (Campbell et al., 1994). In this area, the greenstone sequence consists of massive and pillowed lavas, agglomerates, minor carbonate sediments, a cherty iron-formation and very minor shale and marl layers. The approximately north-south trending greenstones dip steeply to the west. To the east, the greenstones are bounded by intrusions of gneissic granite and a younger quartz porphyry. To the west, they are covered by rocks of the Karoo Supergroup.

To the east of Turk Mine, several discontinuous bands of stromatolitic carbonate sediments are developed. Macgregor (1937) first described these carbonates and documented stromatolites at the Huntsman quarry exposure. The carbonate sequence is generally dolomitic and is preserved as lensoid bodies along the contact between the metabasalts and the quartz porphyry (Fig 2). The carbonate rocks occur as relatively thin

discontinuous layers, with a maximum thickness of approximately 300m, and a maximum strike length of several kilometers. In the area of the Turk Mine the contact between the carbonate rocks and the metabasalts is usually characterized by the presence of a ferruginous, cherty horizon that has been mapped as banded iron formation. To the south of Turk Mine this layer extends as a persistent horizon for some 20km (Fig 2). To the north of Turk Mine, the cherty unit is less persistent and in the northernmost section it does not occur as a continuous horizon, but rather as numerous small lenses distributed within the carbonate rocks, or along the contact between the sediments and the adjoining metabasalts (Fig. 2). This iron-formation-carbonate sediment association is very similar to that described for the Manjeri Formation, which occurs at the base of the Upper Bulawayan Group in the Belingwe Belt, where a persistent layer of predominantly sulphide facies banded iron-formation overlies discontinuous carbonate layers (Wilson, 1981). This possible lithological correlation suggests that these layers just to the east of Turk Mine may mark the base of the greenstone succession in this area. Thus, the greenstones exposed to the east of this are likely to represent a higher structural level within the Upper Bulawayan Group that have been overthrust by the rocks to the west of the banded iron-formation. Consequently, a significant thrust fault must be associated with the banded iron-formation ridge. The banded iron-formation, the carbonate sequence and the Turk Mine are located in the hanging wall of this thrust fault. This interpretation appears to be supported by the strong shear fabric developed in the banded iron-formation in the area of Turk Mine.

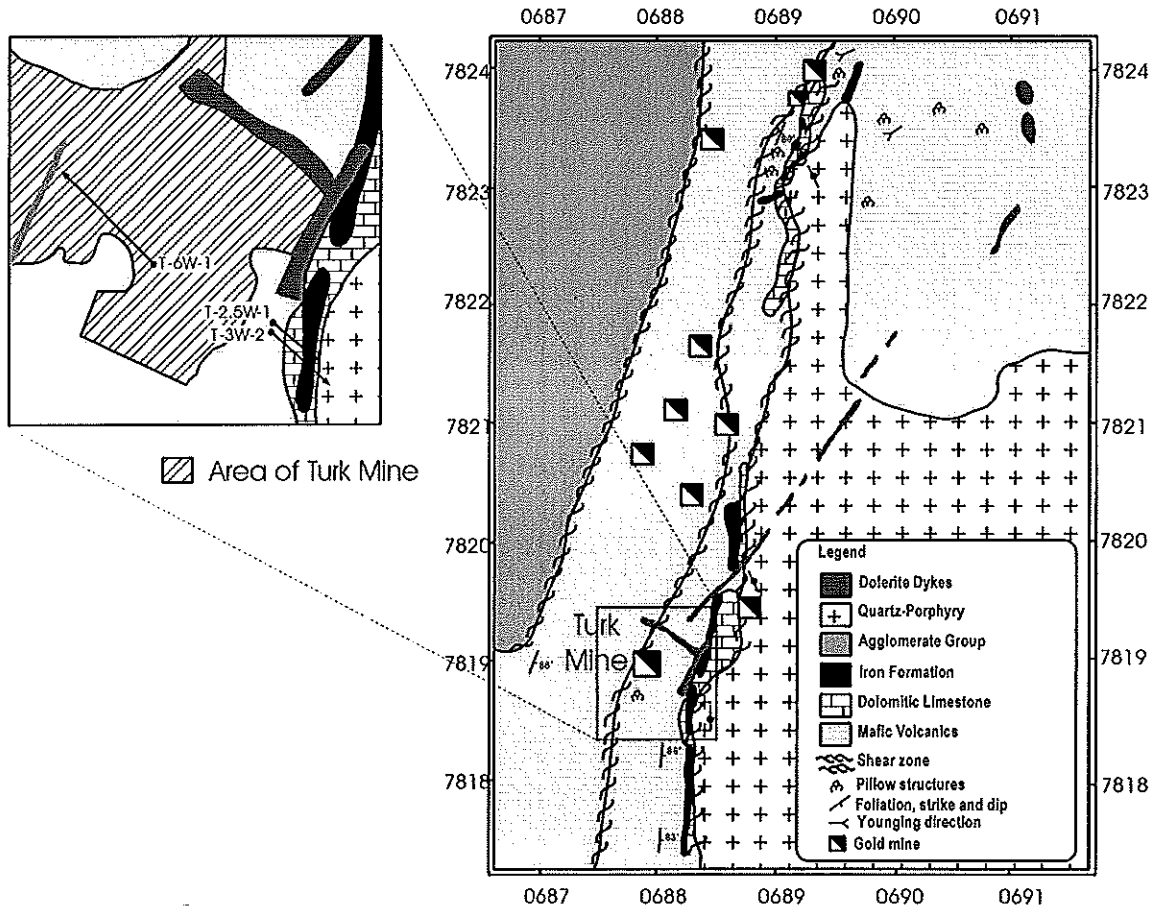


Figure 2: Geological map of the area surrounding Turk Mine (After Dziggel et al., 1998)

BOREHOLE LITHOLOGICAL SEQUENCE

Samples were chosen from two borehole cores through the carbonate sequence (T2 and T3) and from a single borehole core in the main Turk deposit (T6).

Carbonate Sequence

Both borehole cores, T2 and T3, expose an identical succession of metabasalts, dolomitic carbonate sediments and sheared intrusive quartz porphyry (Fig. 3). The metabasalts consist of both massive and pillow varieties.

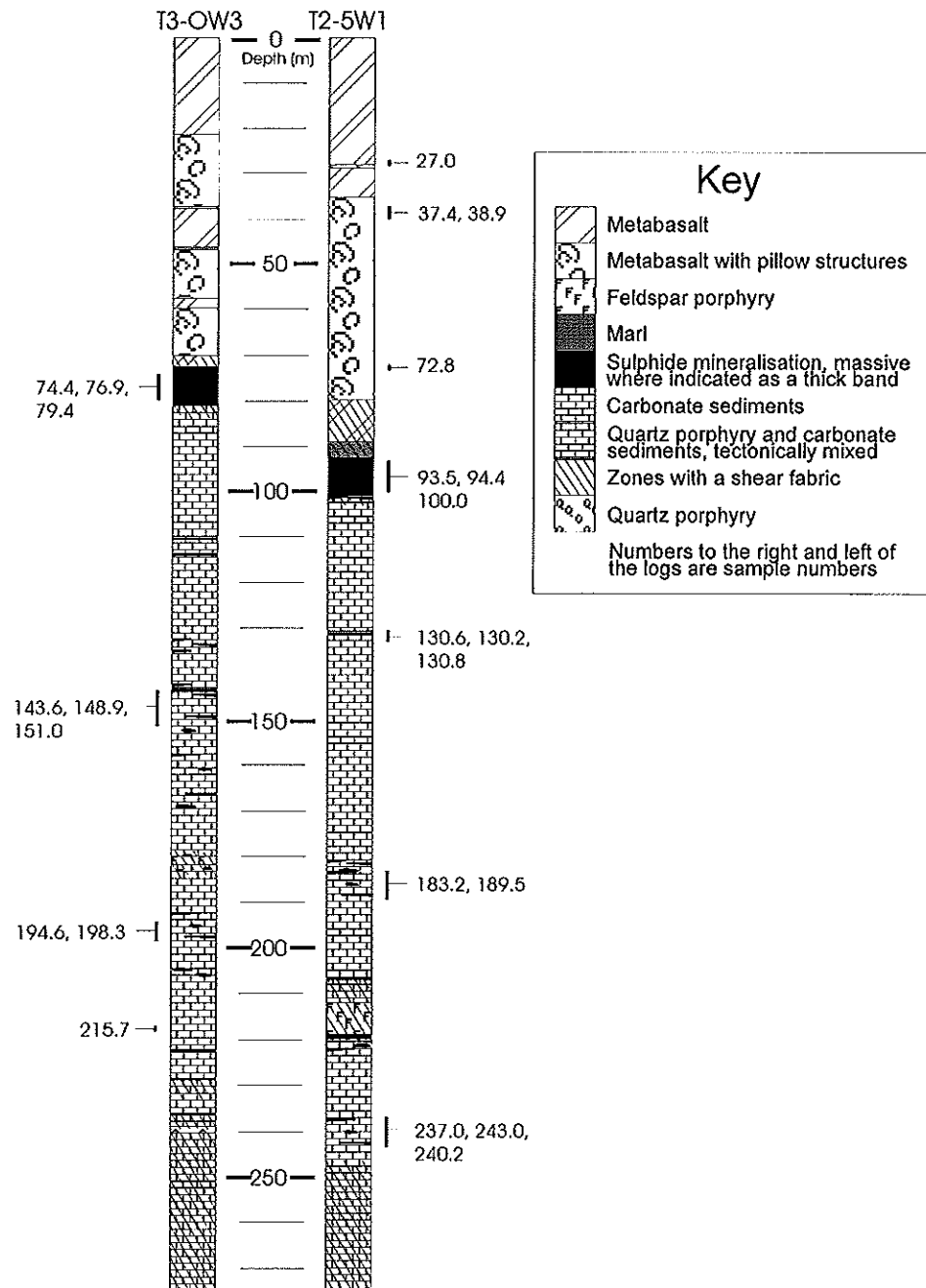


Figure 3: Logs for borehole cores T3-OW3 and T2-5W1 from the carbonate sequence east of Turk Mine.

In general, a shear fabric is developed towards the base of the metavolcanic sequence. This may have resulted in the original pillow structures within this zone being destroyed due to the high degrees of strain. The metabasalts are underlain by approximately 150m of dolomite containing inhomogeneously distributed sulphide mineralization. This mineralization is mostly focussed on brecciation zones which characterize the carbonate sequence in both boreholes. In these zones the fragments are often dark magnesian carbonate with a white calcite matrix. In some areas the clasts consist of shale and marl layers with the same matrix. Shear fabrics are generally not developed in the breccia zones. The breccias are therefore interpreted to have formed during slumping of semi-lithified carbonate and marl layers. The lack of shearing has resulted in the preservation of delicate small-scale sedimentary features such as finely laminated bedding in marl clasts, stromatolitic features in carbonate clasts and ooids in carbonate clasts.

The carbonate sequence is truncated by the quartz porphyry intrusion. The major lithological contacts are the focus of shear zones and strongly developed shear fabrics characterize both the metabasalt-carbonate contact and the carbonate-porphyry contact. Within the metabasalts and the carbonate sequence there are a number of minor dyke-like intrusions of feldspar porphyry with a maximum thickness approaching 5m. These intrusions are also generally the locus of shearing. In addition to the feldspar porphyry intrusions occasional marl layers occur in the metabasalts.

Turk Deposit

The borehole core from the Turk deposit displays both massive and pillowd metavolcanic units interspersed with zones of quartz-carbonate alteration (Fig. 4). The upper 100m of the core consists predominantly of pillow lavas with relatively minor and thin partings of sheared quartz-carbonate alteration zones. Between 100m and 315m the core comprises predominantly metavolcanic rock showing quartz-carbonate alteration interspersed with undifferentiated zones of unaltered metavolcanic rock. Below 350m the core consists of felsic dykes interlayered with banded shales and iron formation.

Pyrite-bearing Zones

Pyrite is the only sulphide mineral that has been noticed in this study. In the borehole cores T2 and T3, the pyrite-bearing zones are confined to the carbonate sequence and to the carbonate-metabasalt contact. Within the carbonate sequence pyrite is most commonly developed within brecciated zones. In these zones, pyrite mineralization pseudomorphs small-scale sedimentary structures.

Pyrite also occurs in association with shear zones. These are best developed at the lithological contacts bounding the carbonates. A zone of massive pyrite development, which on surface weathers to produce well-defined gossanous zones, marks the contact

with the metabasalts. Along strike these areas of massive sulphide development are truncated by silica-rich areas, which have the appearance of sheared cherts. These zones also contain substantial amounts of pyrite. The contact between the carbonates and the quartz porphyry is also sheared, although in this area the shear fabric is more diffusely developed in approximately 10m of core. In this zone the porphyry and carbonate rocks are tectonically mixed. In borehole T6, pyrite is developed in the sheared and altered zones of the metavolcanics.

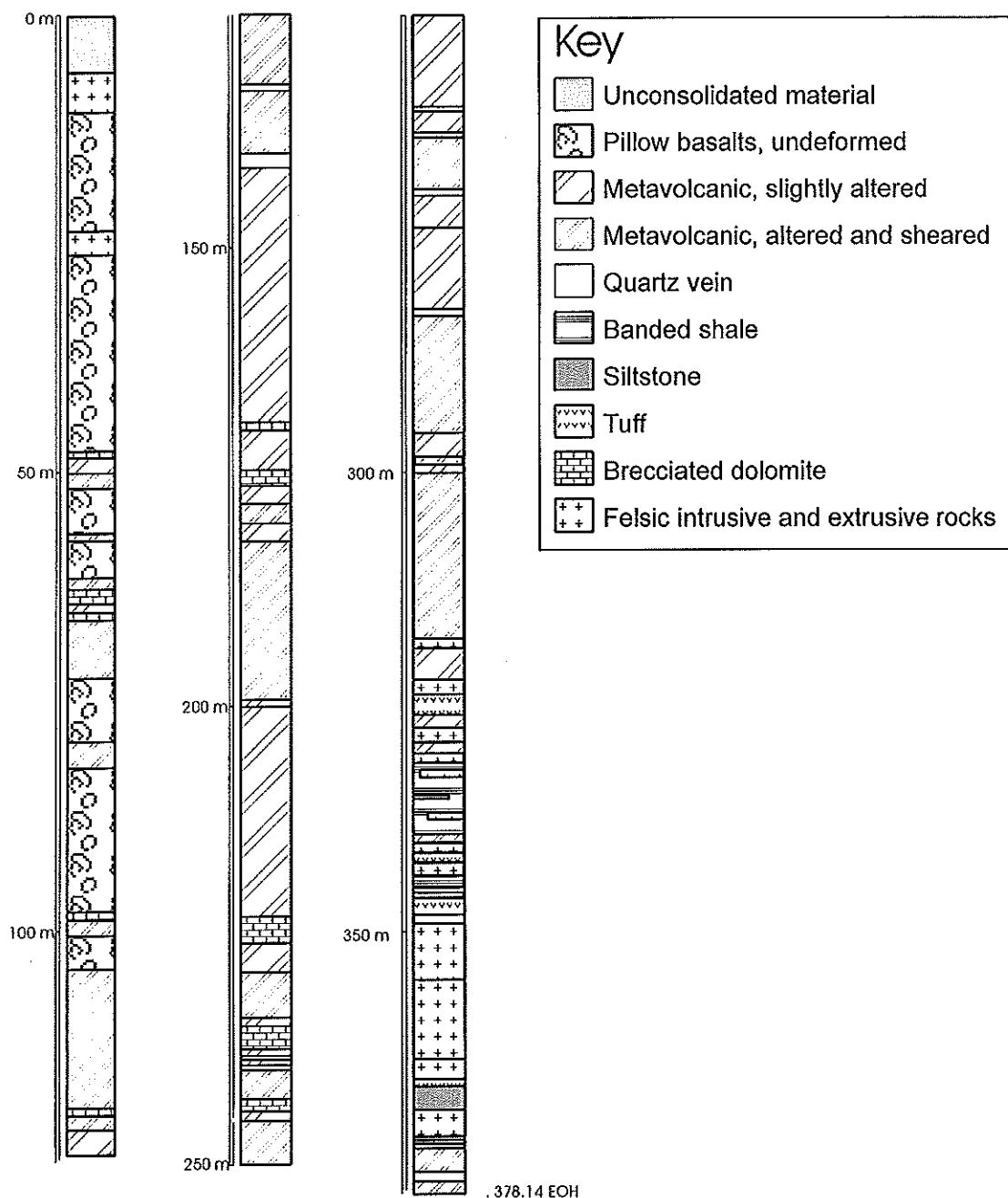


Figure 4: Logs for the T-6W-1 borehole core from the metavolcanics of the Turk Mine deposit. The core displays a metavolcanic sequence with varying amounts of shearing and quartz-carbonate-pyrite alteration (After Dziggel et al, 1998)

PETROGRAPHY

All the samples from the boreholes have been subjected to detailed petrographic study. The main aim of this exercise has been to characterize the pyrite textures within the carbonate sequence and within the altered metavolcanics.

Pyrite Textures in the Carbonate Sequence

Several textural varieties of pyrite occur in the carbonate rocks. These have been subdivided into sedimentary pyrite clasts, pyrite which pseudomorphs Fe-rich sedimentary features, individual euhedral pyrite crystals, and zones of massive pyrite development. The characteristics and setting of these different pyrite generations are discussed below.

Pseudomorphic Pyrite

This textural category includes several pyrite types formed through pseudomorphing sedimentary features in both the carbonates and in shale and marl clasts in the breccia zones. Typical examples of replacement features in the carbonates include small, rounded, pyrite structures ranging in diameter from 2 to 6mm. These structures have cores of porous pyrite, often exhibiting a concentric banding pattern (Fig. 5), and are interpreted to be the result of pyrite replacement of the Fe-rich portions of ooids.

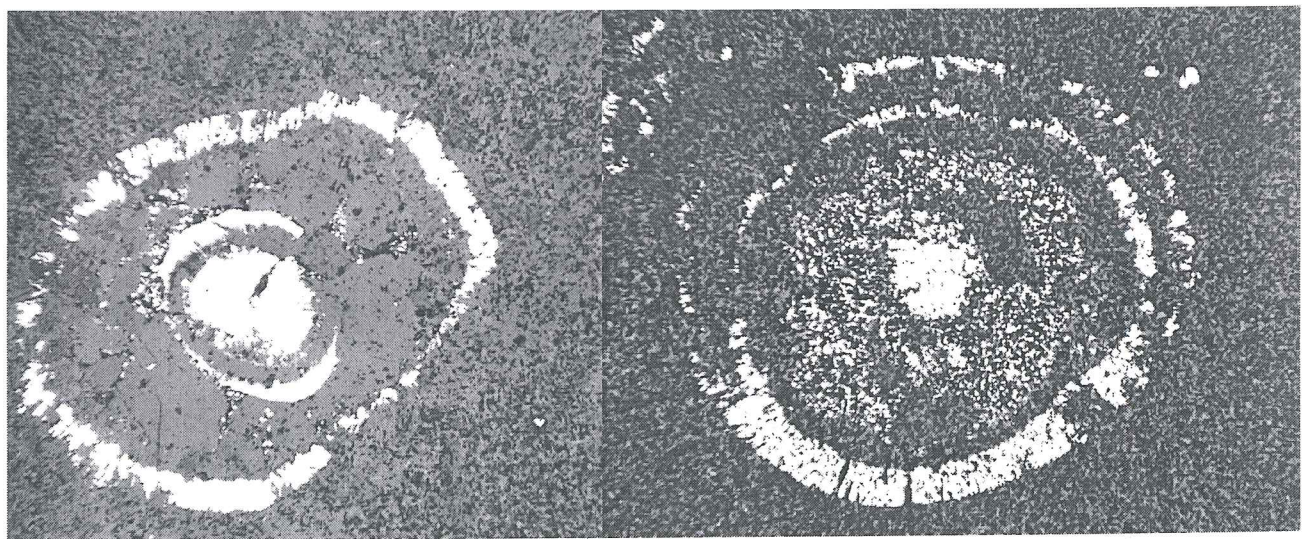


Figure 5: Microphotograph of pyrite pseudomorphing a sedimentary ooid structure. These structures have cores of porous pyrite and rims of radiating pyrite crystals surrounding the cores. Often, towards one side of the structure, a small pyrite-free area separates the rim and core. These structures are considered to have formed through the replacement of ankerite-rich zones in carbonate ooids. Similarly, Fe-rich zones within stromatolites are also commonly replaced by pyrite. Pyrite replacement of carbonate sedimentary features is common in the breccia horizons, but has also occurred within the general carbonate succession, particularly close to minor shear zones.

Pyrite Clasts

The pyrite clasts consist of rounded aggregates of blocky pyrite crystals, typically approximately 5 mm in diameter (Fig. 6), and occur only in the breccia horizons. The rounding of these clasts is interpreted to have resulted from abrasion at the time of formation of the breccia. The formation of the pyrite crystals in these clasts therefore predates the deposition of the breccia.

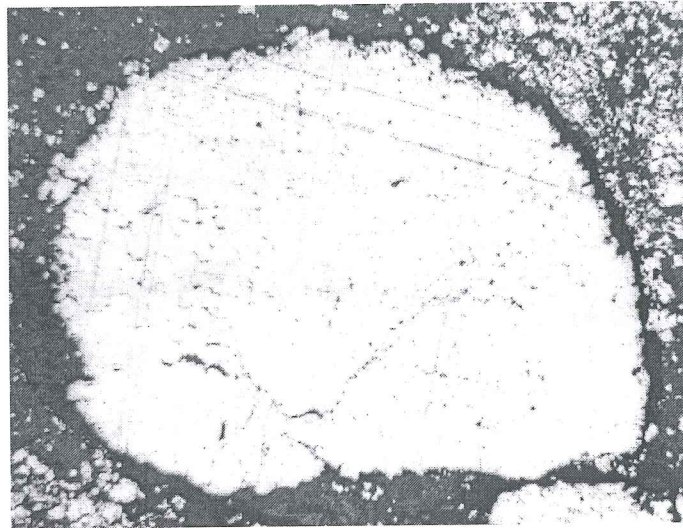


Figure 6: Microphotograph of a pyrite clast consisting of rounded aggregates of blocky pyrite crystals. This pyrite generation seems to predate the porous pseudomorphed sedimentary structures.

Euhedral Pyrites

In all areas of pyrite development within the samples individual euhedral pyrite crystals occur in addition to the other pyrite types. Euhedral pyrite occurs as two distinct varieties; as individual euhedral crystals within fractures and veins (Fig. 7) and as accumulations of inclusion-rich euhedral crystals within the breccias (Fig. 8), where such pyrite crystals can form a substantial proportion (> 40%) of the matrix. Clearly, in both cases, these crystals have grown after the formation of the breccias.

Massive Pyrite

This pyrite variety is confined to the sheared carbonate-metabasalt contact. Where undeformed, it has a coarsely crystalline texture and occurs as large blocky masses. However, this part of the succession is intensely sheared and the pyrite crystals have commonly undergone brittle fracture associated with the development of a prominent shear fabric.



Figure 7: Microphotograph of euhedral pyrites crystals as seen in fractures or in veins within the carbonate sequence.

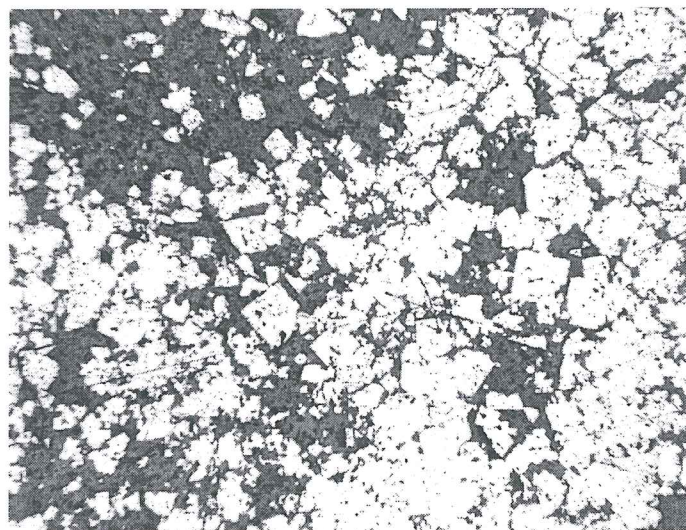


Figure 8: Microphotograph showing the texture typical of the poikiloblastic euhedral pyrite generation.

Pyrite Textures in the Metavolcanics

Compared to the complex pyrite generations in the carbonate sequence, the pyrites in the metavolcanics are simple. In samples examined in this study a single pyrite generation was identified which occurs as euhedral crystals within the quartz-chlorite-carbonate matrix (Fig. 9). Locally, where late shear fabrics are developed, these pyrite crystals become brecciated through cataclastic deformation processes (Fig. 10).



Figure 9: Microphotograph from the T-6W-1 borehole core illustrating the large euhedral pyrite crystals from the metavolcanic sequence of the Turk deposit.

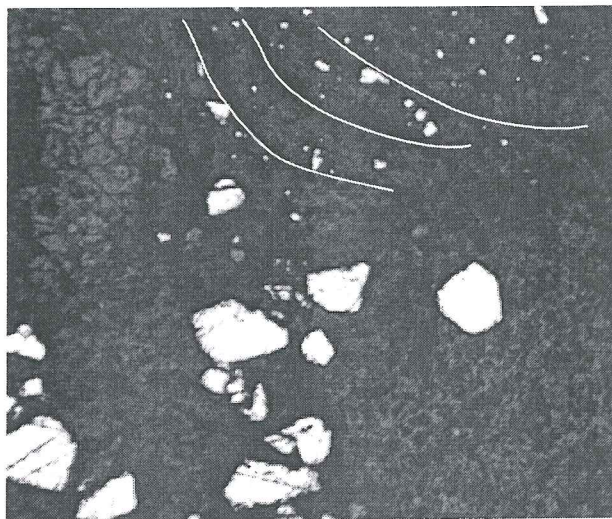


Figure 10: Microphotograph showing the brecciation of large, euhedral, pyrite from the Turk deposit as the result of a shearing event which postdates the quartz-pyrite-carbonate alteration.

SULPHUR ISOTOPE ANALYSES

Sulphur isotope analyses ($\delta^{34}\text{S}$) were conducted on pyrites extracted from the pyritic zones within T2 borehole core, the aim being to constrain the environments of deposition for the complex pyrite generations in these samples.

Laboratory Technique

The samples selected for stable isotopic analysis were crushed and the pyrite crystals were separated by hand-picking. The pyrite aggregate from each sample was ground into a

fine powder using a agate mortar and pestle and prepared for the gas extraction line by mixing ± 9 mg of sample material with ± 200 mg of copper-oxide. The samples were placed into the gas extraction line, evacuated and heated to 1000 °C for 30 minutes to allow for complete degassing of the sample. The SO₂ extraction process involved a number of steps: (1) any H₂O in the gas fraction was trapped using propanol cooled to -60 °C by addition of liquid nitrogen; (2) SO₂ and CO₂ were simultaneously frozen in using a liquid nitrogen trap; (3) these gases were separated using an ethanol trap, cooled to -113 °C by the addition of liquid nitrogen. At this temperature CO₂ is liberated and pumped away, while SO₂ remains frozen in; and, (4) SO₂ is transferred to the collection tube using a liquid nitrogen trap where it is sealed by melting off the neck of the tube. The sulphur isotope ratios of the extracted gases were determined via the mass spectrometer at the Council for Geoscience in Pretoria by Dr P.A. de Groot.

Sulphur Isotope Ratios and Results

The sulphur isotope ratios for 15 samples are presented in Table 1 and illustrated in Figure 13. The results include one duplicate analysis and two δ³⁴S determinations on a stibnite standard. The δ³⁴S values for the duplicate analyses are within a range of 0.4 ‰; those of the stibnite standards fall within a range of 0.1 ‰. Within this error, the δ³⁴S values determined for the stibnite standard are identical to the known composition of the standard. The δ³⁴S values for the data set range from approximately 15 to -3,00 (Fig.11).

Table 2: Sulphur isotope ratios for the pyrite-bearing samples of the carbonate sequence from the T2 borehole core

Sample #	T2.240.2	T2.240.2	T2.183.2	T3.215.7	T3.179	T2.96.94	T2.130.6	T2.237
S (g)	8.92	X	8.63	8.12	9.09	9.09	9.24	10.08
co (g)	200.4	X	202.6	200.5	201.08	200.3	208.4	203.75
CO ₂	17.21	20.1	35.64	22.46	28.72	16.09	10.33	14.13
SO ₂	>100	>100	83.36	71	63.6	>100	107.8	>100
δ ³⁴ S	15.445	15.08	-2.11	1.93	-1.66	-2.75	-0.11	13.1

Sample #	T2. 243	T2.189	T2. 94.4	T2.130.2	T2. 94.2-	GS1-	GS1-
S (g)	8.28	8.68	8.26	8.5	8.16	10.96	15.85
co (g)	202.8	202.3	199.1	200.1	205	207.7	207
CO ₂	22.02	21.92	6.74	19.62	6.21	3.03	4.25
SO ₂	>100	>109.6	>100	>100	99.1	40.6	63.58
δ ³⁴ S	6.94	3.91	-0.59*	-3.9	-3.07	2.21	2.26

When interpreting these results it must be considered that during sample preparation, the different pyrite generations were not separated. Thus, the results probably represent a mixture of the sulphur isotopic compositions. An attempt was made to correlate the

petrography of each sample with the $\delta^{34}\text{S}$ value obtained (Fig.12).

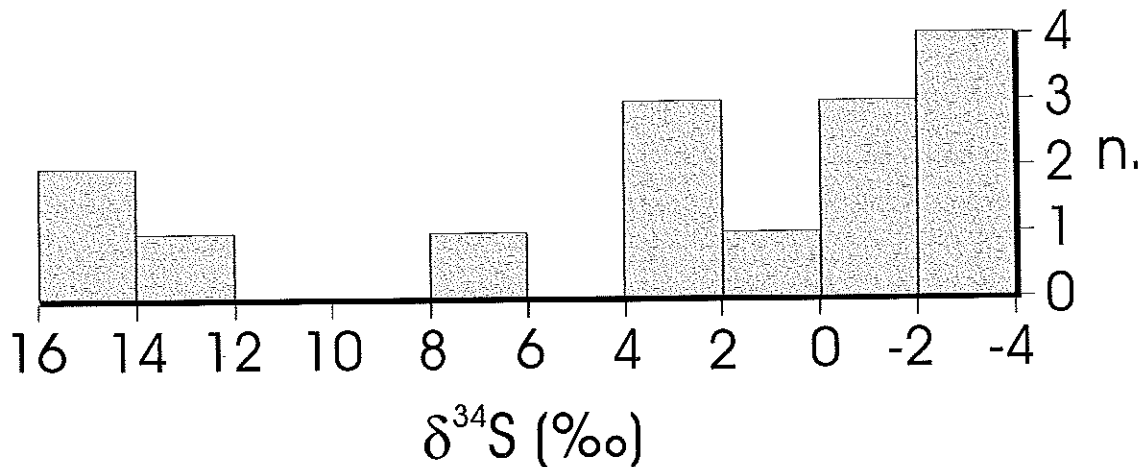


Figure 11: Graph illustrating the results from the sulphur isotope analysis, with the number of samples plotted against the $\delta^{34}\text{S}$ values. The graph also indicates the results for the stibnite laboratory standards.

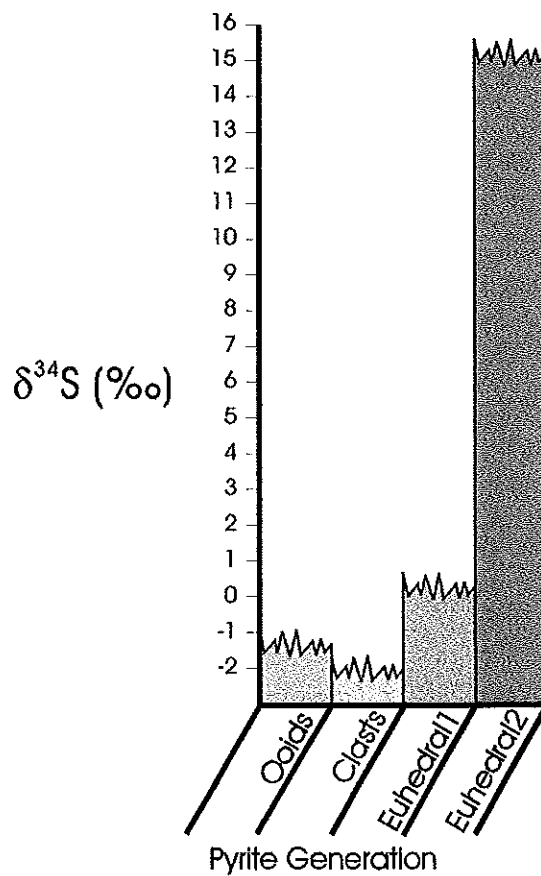


Figure 12: Graph illustrating the different pyrite generations plotted against the $\delta^{34}\text{S}$ ratios. The data support the interpretation that sulphur in pyrite from the pseudomorphed sedimentary structures, in euhedral pyrite from veins and fractures (Euhedral 1), and in pyrite clasts, is of magmatic origin. That in the euhedral poikiloblastic pyrite (Euhedral 2) appears to be of sedimentary origin.

Samples dominated by massive pyrite, pseudomorphic pyrite and euhedral pyrite in veins produced $\delta^{34}\text{S}$ values of 0 or less. Given the geological context of these sediments, these values are interpreted as reflecting sulphur derived from a magmatic source. The massive pyrite, which is developed at the boundary between the carbonate sediments and the overlying metavolcanic sequence, may represent pyrite produced at vents or pyrite accumulations crystallized from solutions migrating along this lithological boundary. The pseudomorphic pyrite and the euhedral vein pyrite are interpreted to have crystallized from solutions containing sulphur of magmatic origin.

According to Ohmoto et al. (1993), $\delta^{34}\text{S}$ values between 0 and 6 are typical of sedimentary rocks from the Archaean. This study has revealed a large spread of positive $\delta^{34}\text{S}$ values from 0 to > 15 . This probably reflects mixtures, in varying ratios, of the previously discussed pyrite generations with pyrite formed from sulphur of sedimentary origin. Thus, these positive $\delta^{34}\text{S}$ values are interpreted to reflect an input of sulphur derived from sulphate minerals. Sulphate is the second most abundant anion in present day seawater (Ohmoto et al., 1993), allowing pyrite to form directly in Fe-bearing anaerobic sediments where SO_4^{2-} , supplied from the surrounding seawater, is converted to H_2S by SO_4^{2-} reducing bacteria (Ohmoto et al., 1993).

All the samples that produced $\delta^{34}\text{S}$ values of > 3 contained a significant proportion of the poikiloblastic euhedral pyrite generation (Fig. 8). Sample T2-240, which produced the most positive $\delta^{34}\text{S}$ value, is dominated by this pyrite generation. Consequently, this pyrite type is interpreted to have formed through a process involving bacterial reduction of sulphate minerals. Studies by Ohmoto et al. (1993) on pyrite-bearing sedimentary horizons in the Barberton greenstone belt have identified pyrite with $\delta^{34}\text{S}$ values as high as 8 %. These pyrites were interpreted to have formed through the bacterial reduction of seawater sulphate at approximately 3.4 Ga. The Bubi greenstone belt has an age of ± 2.7 Ga, and it is therefore proposed that at this time sulphate-reducing bacteria were present in the marine environment in which the carbonate sediments were deposited.

PROTON INDUCED X-RAY EMISSION (PIXE) ANALYSES

The micro-PIXE elemental mapping and point analyses were made using the nuclear microprobe at the National Accelerator Centre (NAC) at Faure (near Cape Town), South Africa. This microprobe is based on a 6 MV single-ended Van de Graaff accelerator. Details of the instrument and beam focusing techniques are given in Prozesky et al. (1995) and Churms et al. (1993).

A resolution in the order of 1 μm beam spot size is achievable for proton currents of 100 pA. Currents in the order of 10 nA result in beam spot sizes not exceeding 10 μm . For the present study a 3 MeV proton beam was used, focused to $5 \times 5 \mu\text{m}^2$ and rastered over

areas between $0.3 \times 0.3 \text{ mm}^2$ and $1.6 \times 1.6 \text{ mm}^2$, depending on the grain size of analysed pyrites. Beam current was kept between 1 and 2 nA to avoid count rates exceeding 3000 c/s. The X-rays were detected using a Link Pentafet Si (Li) detector positioned at 135 degrees with respect to the incident beam, using a $150 \mu\text{m}$ thick Al absorber. The total accumulated charge for the rastered areas varied between 2.4 and $50 \mu\text{C}$, and for point analyses it was either 0.5 or $1 \mu\text{C}$. PIXE spectra were analysed using the GeoPIXE suite of programs (Ryan et al., 1990a, b). A detailed study on the accuracy and precision of the PIXE system was reported by Van Achterberg et al. (1995). Elemental maps were obtained using a rapid matrix transform method called Dynamic Analysis (DA), which is a part of GeoPIXE package (Ryan et al., 1993; 1995). The images are inherently overlap-resolved, background subtracted and the maps are generated on-line. Final maps give quantitative elemental images with the intensity in ppm. This method was thoroughly tested for geological applications (Przybylowicz et al., 1995; Ryan et al., 1996). Scanned regions were divided into 64×64 pixels, with scanning speed 10 ms/pixel. The final maps are contours linking pixels with similar values and are presented using programs written in the Interactive Data Language.

Pyrite Geochemistry

The elemental maps of pyrite (Fig. 13) clearly show a different geochemical signature for each pyrite generation identified in the carbonate sequence. The distribution of arsenic, which is incorporated into the pyrite structure as an arsenopyrite component, is particularly interesting. The data shows that the porous, biogenic pyrite structures (pseudomorphed ooids, stromatolite layers) crystallized in an environment of relatively high arsenic concentration. Arsenic is typically a mobile element during low temperature geological processes and this is possibly consistent with the interpretation of these pyrites having formed during the migration of exhalative-derived hydrothermal fluid through the porous, brecciated sedimentary horizons. The chemical zonation patterns in these structures (Fig. 13d) suggest a two-stage growth process, where arsenopyrite-rich cores (the most porous parts of the structure) are surrounded by rims of almost pure pyrite (corresponding to a radial recrystallization texture). Antimony and lead concentrations are also significantly elevated in the zone of arsenic enrichment (Table 2). Chalcopyrite shows no meaningful association with the arsenic-rich zones.

The pyrite clasts show an inverse zonation of the arsenopyrite component relative to that demonstrated by the ooids (Fig. 13e). The rims of the clasts are weakly enriched in arsenic relative to the cores (Table 2), although texturally there is no difference in the pyrite crystals in the rims and cores of these structures. This could indicate partial equilibration of the rims of these clasts with the fluid from which the porous pyrite structures were precipitated. The chalcopyrite component in these crystals is randomly distributed and the copper concentrations are low.

Figure 13:

13a and 13b: True elemental maps of Fe, As and Au in a section of sample T6W. The larger euhedral pyrites are truncated by a micro-shear, which post-dates the main quartz-carbonate-pyrite alteration assemblage resulting in the brecciation of the pyrites. The curved shear fabric is developed in the top half of the images. The large euhedral pyrites are present in the lower left quadrant (see Figure 10 for a clearer image of the same area of this sample). The maps indicate that the gold is associated with these micro-shears.

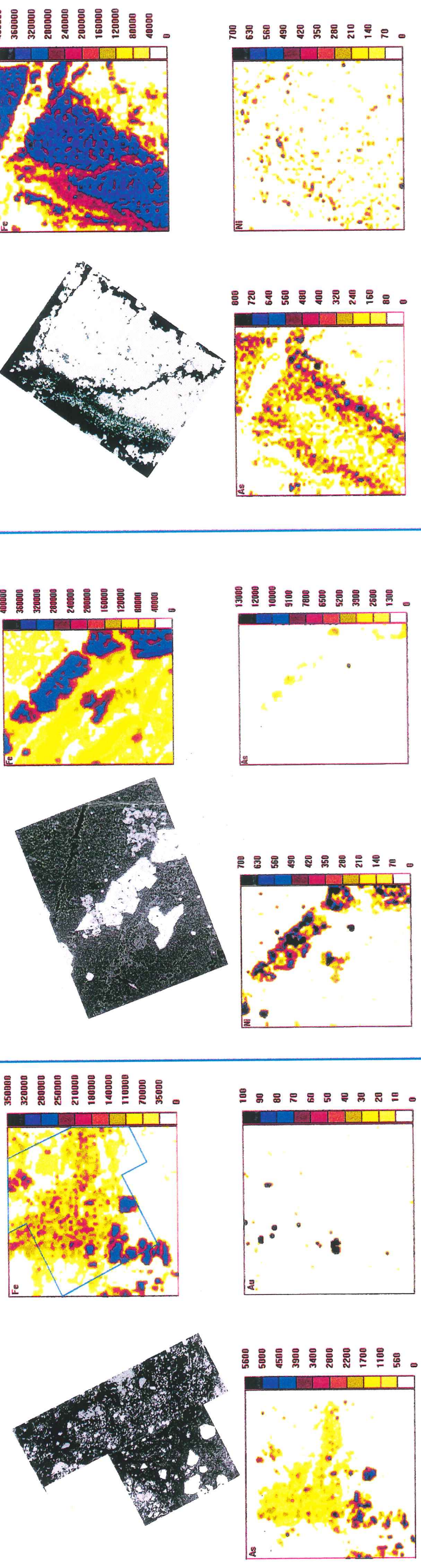
13c: True elemental maps showing the distribution of Fe, As and Ni in the euhedral pyrites observed within the fractures and veins of the carbonate sequence.

13d: True elemental maps showing the distribution of Fe, As and Ni in the pseudomorphed sedimentary structures within the carbonate sequence. The maps show a zonation with respect to arsenic suggesting a two-stage growth process, where the cores of the structures formed in an As-rich environment.

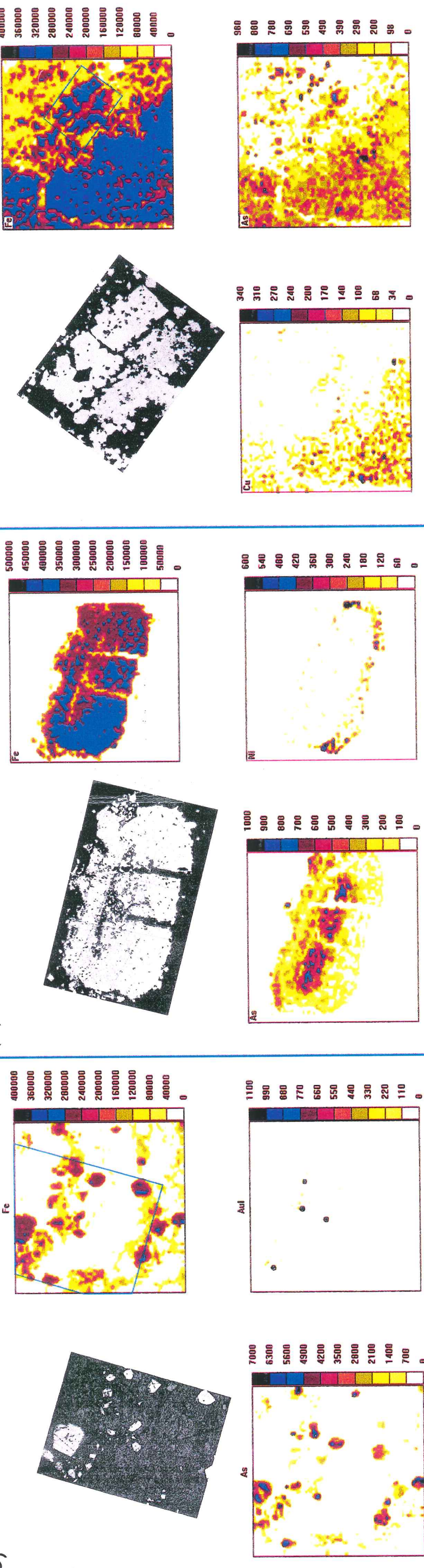
13e: True elemental maps of Fe, Ni and As distribution in pyrite introduced into the breccias as sedimentary clasts. From the maps it appears that the pyrite clasts partially equilibrated with an As-bearing fluid, resulting in the As-enriched rim.

13f: True elemental maps showing the distribution of Fe, Cu and As in the euhedral poikiloblastic pyrites of the carbonate sequence (see text for a more detailed discussion of the pyrite geochemistry).

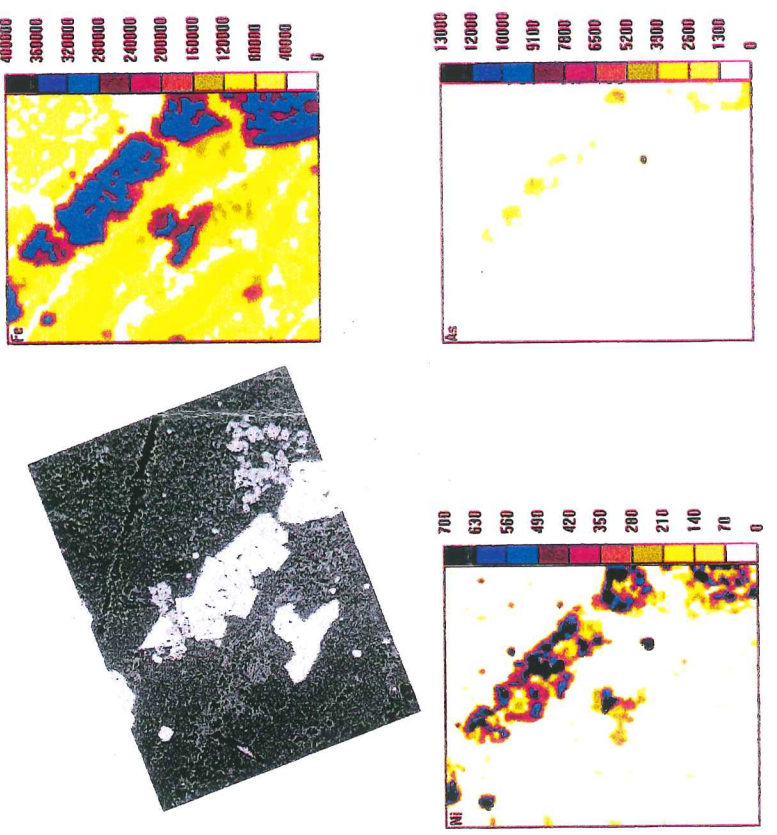
(a)



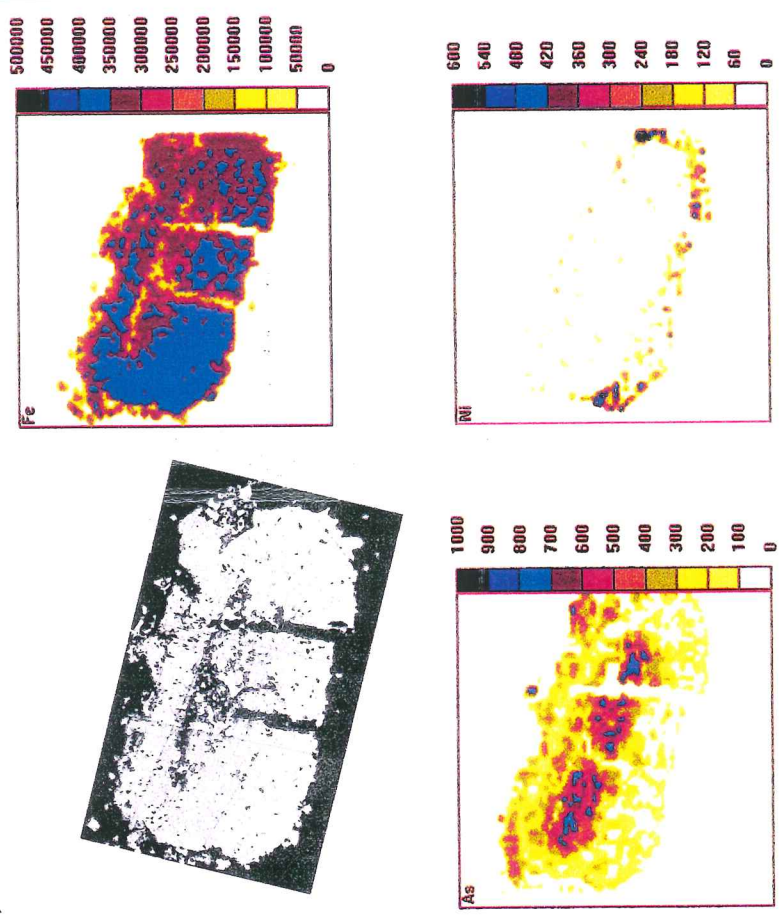
(b)



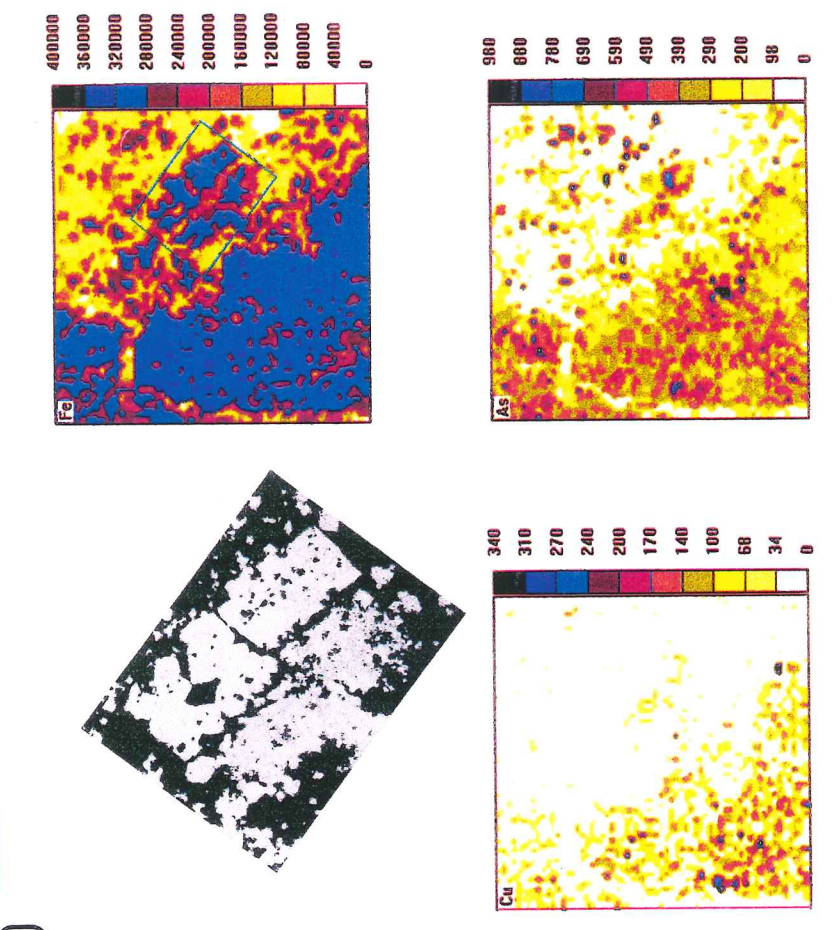
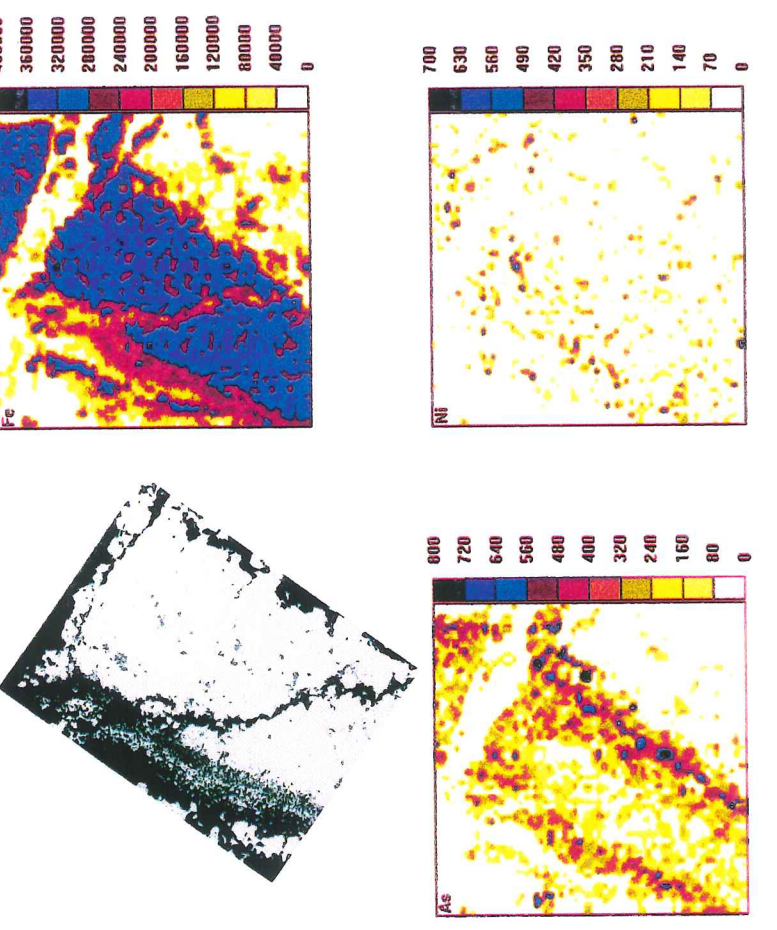
(c)



(d)



(e)



The poikiloblastic euhedral pyrite (Fig. 13f) has very low trace element concentrations (Table 2), and these show no systematic zonations. The euhedral pyrite in veins and fractures (Fig. 13c), as well as the pyrite crystals in the zone of massive pyrite development have very high nickel and arsenic concentrations, and low copper and other trace element concentrations (Table 2). Arsenic and nickel are not uniformly concentrated throughout these crystals, but are concentrated into specific zones. The zonation patterns in these crystals are not clear. However, nickel appears to be preferentially enriched in rims surrounding arsenic-rich cores. Geochemically, these pyrite generations are most similar to the pyrite in the altered metavolcanic rocks of the Turk deposit (Table 2). Where shear fabrics are developed within the zone of massive pyrite development there is no evidence for the introduction of copper, arsenic or gold by fluid migration along the shear planes.

All the pyrite crystals analysed from the altered metavolcanics of the Turk Mine deposit have high arsenic and nickel concentrations relative to most of the pyrite generations in the carbonate sequence (Table 2). Arsenic is enriched in randomly orientated discrete zones within these crystals (Fig. 13a, b). These zones may represent earlier-formed arsenic-rich pyrites that have been overgrown during the crystallization of the euhedral pyrite generation. Other trace element concentrations are low (Table 2), except for silver and gold which are markedly concentrated in discrete zones (Fig. 13a, b).

Gold Introduction

The data from the carbonate sequence indicates arsenic enrichment in the early, porous pyrite generations. Arsenic and gold concentrations are commonly positively correlated in many gold mining provinces and, consequently, a tentative case may be made gold introduction early in the paragenetic sequence in these rocks. Unfortunately, gold concentrations in all the pyrites examined from the carbonate sequence were either below or very close to detection limits (Table 2) and as a result, no conclusive findings can be made in this regard.

Following the PIXE study, the gold, copper, nickel, arsenic, sulphur and silver contents of the samples from boreholes T2 and T3 were determined by standard assay techniques. The analyses were conducted by Bergstrom & Bakker Laboratories (Johannesburg) on small carbonate samples averaging 50 g (Table 3). The data indicate relatively low levels of gold enrichment in the samples studied, with the highest gold concentration being approximately 0.4 ppm. Thus, gold in these samples is either present at levels below the detection limit of PIXE mapping, or is concentrated into micro-domains which were not present in the areas analysed during this study. The gold grades recorded in weathered surface samples of these rocks by Casmyn Mining geologists probably reflects a supergene enrichment process.

Table 2: PIXE spot analyses of trace element concentrations in pyrites from the carbonate sequence and from the Turk deposit. Concentrations and errors are in ppm. The sample numbers correspond to borehole depth (Figs. 3, 4)

	ooid				ooid		clast				Poik. Eu.
	T2.189.5				T3.74.4		T2.183.2				T2.183.2
	rim	rim	core	core	rim	core	core	core	rim	rim	p1
Ni	389.0	334.0	406.0	417.0	397.0	145.0	171.0	162.0	350.0	307.0	56.1
Cu	159.0	124	220.0	287.0	43.6	74.3	98.8	105.0	178.0	98.1	bd
Zn	bd	bd	bd	bd	bd	bd	bd	bd	Bd	bd	bd
As	314.0	316.0	917.0	1187.0	342.0	696.0	173.0	215.0	424.0	266.0	21.5
Se	22.8	bd	19.0	10.0	bd	6.3	bd	bd	Bd	6.7	14.6
Ag	11.5	bd	18.5	34.1	bd	bd	bd	bd	Bd	bd	bd
Sb	46.9	32.1	172.0	305.0	29.9	260.0	30.8	41.9	98.2	45.8	bd
Au	bd	bd	bd	bd	bd	19.3 ± 6.87	bd	Bd	bd	bd	bd
Pb	43.3	bd	218.0	350.0	26.0	137.0	bd	bd	Bd	bd	bd

	ooid				clast				Poikiloblastic Euhedral			
	T3.148.9a				T3.148.9b				T3.151			
	rim	rim	core	core	rim	rim	core	core	core	p1	p2	p3
Ni	128.0	208.0	220	269.0	107.0	101	98.3	127.0	175.0	451.0	795.0	81.5
Cu	21.1	112.0	88.5	99.6	70.5	bd	35.3	78.1	78.3	18.2	n/a	bd
Zn	bd	bd	bd	bd	bd	bd	16.7	bd	Bd	bd	bd	bd
As	314.0	457.0	565	508.0	812	319	298	231.0	233.0	121.0	951.0	188.0
Se	7.56	bd	10.2	bd	12.8	bd	bd	bd	Bd	13.5	19.9	8.5
Ag	bd	bd	bd	n/a	bd	bd	7.94	bd	N/a	bd	12.0	n/a
Sb	21.4	93.7	212.0	171	38.6	37.8	59.2	44.7	30.9	69.4	33.7	59.2
Au	bd	bd	bd	n/a	bd	bd	bd	Bd	bd	bd	n/a	bd
Pb	bd	bd	154.0	136.0	n/a	n/a	bd	bd	Bd	bd	n/a	bd

	Euhd. Vein	Turk Deposit – Euhedral Pyrite						Turk Deposit – Brecciated Pyrite			
	T2.130.2		T6w.1.90a				T6w.1.90b				
	p1	p2	p1	p2	p3	p4	p5	p1	P2	p3	p4
Ni	1330.0	1030.0	305.0	1170.0	1290.0	1220.0	1370.0	747.0	1190.0	676.0	1150.0
Cu	bd	bd	bd	bd	46.6	694.0	278.0	4220.0	266.0	77.2	65.8
Zn	n/a	n/a	64.6	n/a	bd	14.5	88.5	n/a	206.0	102.0	149.0
As	6250.0	1310.0	5860.0	5890.0	4280.0	2770.0	243.0	1230.0	1850.0	140.0	20100
Se	20.4	8.22	22.7	27.1	15.6	bd	n/a	n/a	n/a	n/a	n/a
Ag	bd	bd	bd	bd	65.2	18.9	31.4	10000	8040.0	41300	33100
Sb	30.3	n/a	n/a	n/a	bd	39.4	41.5	bd	n/a	bd	bd
Au	27.4	bd	36.5	32.7	294.0	bd	63.3	61100	77400	39400	31400
Pb	±19.2	n/a	n/a	n/a	bd	bd	bd	n/a	bd	bd	bd

	Euhd. Pyrite	Brecciated Pyrite			Brecciated Pyrite			
	T6w.1.90c		T6w.1.90d			T6w.2		
	p1	p2	p1	p2	p3	p1	p2	p3
Ni	563.0	128	703.0	14100	734	15100	151	19000
Cu	bd	bd	257	bd	bd	54300	n/a	
Zn	n/a	n/a	403	116	bd	378	bd	
As	66300	90900	80.3	124.0	745	35700	533.0	92800
Se	28.3	36.3	n/a	bd	n/a	bd	n/a	31.5
Ag	bd	bd	61600	51.8	8940	n/a	551.0	bd
Sb	bd	22.9	n/a	bd	n/a	bd	bd	bd
Au	29.5	49.2	63100	288	62600	bd	52500	bd
Pb	n/a	n/a	n/a	bd	bd	n/a	n/a	

Table 3: Gold, silver, copper, nickel, arsenic and sulphur contents of the samples from boreholes T2 and T3. All values are in ppm except for sulphur where the values are in wt%

Sample #	T2/96.94	T2/94.4	T2/130.2	T2/130.6	T2/183.2	T2/189.5	T2/237.0	T2/240.2
Cu	0	10	15	15	42	18	3	11
Ni	70	26	48	141	165	60	18	71
As	27	28	40	109	244	47	18	72
Au	0.02	0.01	0	0.02	0.42	0.22	0.03	0.15
Ag	0	0	0	0	0	0	0	0
S (wt%)	na	2.94	4.98	2.39	29.5	3.57	0.68	8.74

Sample #	T2/243.0	T3/74.4	T3/76.9	T3/143.6	T3/148.9	T3/179.4	T3/194.6	T3/198.3
Cu	2	15	8	13	8	7	6	16
Ni	40	84	77	137	39	86	54	53
As	44	117	135	132	43	26	106	53
Au	0.02	0.02	0.05	0.06	0.02	0.01	0.38	0.37
Ag	0	0	0	0	0	0	0	0
S (wt%)	9.35	27.0	25.2	28.5	4.74	8.27	12.9	5.15

In contrast to the data from the carbonate sequence, clear evidence exists detailing the process which introduced gold into the altered metavolcanics. This is a function of the generally higher gold content of these samples and the concentration of gold into specific structural sites within the samples. The euhedral pyrite crystals produced by the quartz-carbonate-pyrite alteration have low to negligible gold contents (Table 2). The gold enrichment in the samples has occurred within late micro-shears that clearly post-date this alteration (Fig. 13a, b). The shear fabric into which gold was introduced also occurs as a zone of arsenic enrichment. However, gold and arsenic abundances are inversely correlated at the microscopic level (Table 2). Little to no syn- to post-shearing precipitation of pyrite appears to have occurred in the zones of gold enrichment, as the brecciated margins of the pyrite crystals are preserved. Thus, gold appears to have precipitated on the margins of pre-existing brecciated pyrite crystals and was confined to the area of the micro-shears where the gold-bearing fluid could gain ingress into the rock.

DISCUSSION AND CONCLUSIONS

The geological setting of the samples examined in this study indicates an environment of submarine volcanism post-dating the formation of the carbonate sediments. Hydrothermal fluids produced at such centres typically attain pyrite saturation as they approach the top of the rock pile. Sulphur-bearing fluids derived from this source are likely to have interacted with the potentially porous carbonate breccia horizons as the volcanic

pile was accumulating over, or adjacent to, the carbonate sediments. Reaction between sulphur in these fluids and Fe-rich zones in the carbonates would have produced the pseudomorphing of the delicate sedimentary structures observed in this study. The temperatures attained in such fluids would be lower than those measured at vents (350 to 400 °C) therefore resulting in the very porous-pyrite texture. The pyrite clasts contained within the breccias were potentially derived directly from the environment of the vents during slumping into the carbonate basin, or from pyrite formed within shale and marl layers, which also occur as clasts within the breccias.

Fluid migration during the shearing seen along the lithological boundaries to the carbonate sequence also represents a period of possible pyrite precipitation. Consequently, the massive pyrite developed at the sheared carbonate-metabasalt contact may be of this origin. However, the similarity between the porous textures of these crystals and those produced by pseudomorphing the Fe-rich sedimentary layers suggest a similar origin. Precipitation of these massive pyrite layers may have occurred directly from vented fluid as the pillow lava sequence prograded over the carbonate sequence. This type of chemical precipitation model is supported by the fact that the sulphide-bearing horizon grades directly into a regional ferruginous and cherty band that has been mapped as banded iron formation for tens of kilometers.

The mechanism and relative timing of gold introduction into the carbonate sequence has not been conclusively determined. Primarily, this results from the low gold concentration in these samples, with the consequence that the PIXE study failed to identify individual pyrite generations or zones within crystals that were enriched in gold within these samples. Gold concentrations up to approximately 0.4 ppm were found in samples that were not sheared. These samples did, however, contain several pyrite generations including pseudomorphed ooids, pyrite clasts and poikiloblastic euhedral pyrites. Consequently, it is concluded that in these samples the low levels of gold enrichment are most likely related to the solutions with which the rocks interacted following the formation of the breccia horizons, but are unlikely to have resulted from fluids introduced during shearing.

The samples of metavolcanic ore from borehole T6W examined in this study have considerably higher bulk sample gold contents (up to approximately 11 ppm) than the samples analysed from the carbonate sequence. In all these samples, the euhedral pyrite crystals, which typify the quartz-carbonate-pyrite alteration, have relatively low gold concentrations. High gold concentrations are confined to micro-shear zones along which these large pyrite crystals have become brecciated. Clearly, at least two stages of fluid - rock interaction are involved in the formation of the Turk Mine gold deposit: (1) a relatively early deformation event and fluid influx resulting in quartz + pyrite + carbonate alteration of the chloritic metabasalt; and, (2) a later shearing event, which resulted in the brecciation of the large euhedral pyrite, as well as fluid and gold introduction. During this

shearing event, fluid influx is likely to have been most efficient in zones of brittle deformation, i.e. zones where the prior alteration event had produced a higher proportion of quartz and pyrite. The Turk gold deposit is thus the product of a two-stage fluid influx and alteration process. These findings are supported by a recent study on the altered metabasalts at Turk Mine which attempted to correlate gold concentration with the geochemical signature of the quartz + pyrite + carbonate alteration event (Dziggel et al., 1998). This study demonstrated that gold abundance does not correlate at all with any of the major elements introduced during the formation of the alteration assemblage and also concluded that the ore deposit formed during a two-stage hydrothermal process.

ACKNOWLEDGEMENTS

Support for this research by the Foundation for Research Development is gratefully acknowledged, as is that of Casmyn Mining who provided the sample material. Prof Carl Anhaeusser is thanked for a thorough review which much improved the manuscript. Dr Pier de Groot provided assistance with the sulphur-isotope analyses.

REFERENCES

- Amm, F.L. (1940) The geology of the country around Bulawayo. Southern Rhodesia Geological Survey Bulletin No. 35, 270 pp.
- Condie, K.C. (1981). *Archean Greenstone Belts*. Elsevier, Amsterdam, 434 pp.
- Campbell, S.D.G. and Pitfield, P. E. J. (1994). Structural controls of gold mineralization in the Zimbabwe Craton - Exploration Guidelines. Zimbabwe Geological Survey Bulletin No. 101, 270 pp.
- Churms, C.L., Pilcher, J.V., Springhorn, K.A. and Tapper U.A.S. (1993). A VAX and PC-based data acquisition-system for MCA, scanning and list-mode analysis. Nucl. Instr. and Meth. Vol. 77, pp. 56-61.
- Dziggel, A., Klemd, R. and Stevens, G. (1998). Gold mineralization at Turk Mine, Zimbabwe: geochemical and statistical investigation of the hydrothermally overprinted host rock. Economic Geology Research Unit Information Circular No. 327, University of the Witwatersrand, Johannesburg, 16 pp.
- Macgregor, A.M., Ferguson, J.C. and Amm F.L. (1937). The geology of the country around the Queen's Mine, Bulawayo District. Southern Rhodesia Geological Survey Bulletin No. 30, 175 pp.

- Ohmoto, H., Kakegawa, T. and Lowe, D. R. (1993). 3.4 Billion year old biogenic pyrites from Barberton, South Africa. *Science*. Vol. 262, pp. 555-557.
- Prozesky, V.M., Przybylowicz, W.J., Van Achterbergh, E., Churms, C.L., Pineda, C.A., Springhorn, K.A., Pilcher, J.V., Ryan, C.G., Kritzinger, J., Schmitt, H. and Swart, T. (1995). The NAC nuclear microprobe facility. *Nucl. Instr. and Meth.*, Vol. 104, pp. 36-42.
- Przybylowicz, W.J., Prozesky, V.M. and Meyer, F.M. (1995). True elemental imaging of pyrites from the Witwatersrand Reefs. *Nucl. Instr. and Meth.*, Vol. 104, pp. 450-455.
- Ryan, C.G., Cousens, D.R., Sie, S.H. and Griffin, W.L. (1990b). Quantitative-analysis of PIXE spectra in geoscience application. *Nucl. Instr. and Meth.*, Vol. 49, pp. 271-276.
- Ryan, C.G., Cousens, D.R., Sie, S.H., Griffin, W.L., Suter, G.F. and Clayton, E. (1990a). Quantitative PIXE microanalysis of geological material using the CSIRO proton microprobe. *Nucl. Instr. and Meth.*, Vol. 47, pp. 55-71.
- Ryan, C.G. and Jamieson, D.N. (1993). Dynamic analysis - online quantitative PIXE microanalysis and its use in overlap-resolved elemental mapping. *Nucl. Instr. and Meth.*, Vol. 77, pp. 203-214.
- Ryan, C.G., Jamieson, D.N., Churms C.L. and Pilcher, J.V. (1995). A new method for online true-elemental imaging using PIXE and the proton microprobe. *Nucl. Instr. and Meth.*, Vol. 104, pp. 157-165.
- Ryan, C.G., Van Achterbergh, E., Jamieson, D.N. and Churms, C.L. (1996). Overlap corrected online PIXE imaging using the proton microprobe. *Nucl. Instr. and Meth.*, Vol. 109, pp. 154-160.
- Van Achterbergh, E., Ryan, C.G., Gurney, J.J. and Le Roex, A.P. (1995). PIXE profiling, imaging and analysis using the NAC proton microprobe - unraveling mantle eclogites. *Nucl. Instr. and Meth.*, Vol. 104, pp. 415- 426.
- Wilson, J.F. (1979). A preliminary reappraisal of the Rhodesian Basement Complex. *Spec. Publ. Geol. Soc. S. Afr.*, 5. Pp. 1-23.
- Wilson, J.F. (1981). The granitic-gneiss greenstone shield. B. Zimbabwe, 454-488. In: Hunter, D.R. (Ed). *Precambrian of the Southern Hemisphere*, Elsevier, Amsterdam, 882 pp.
- Wilson, J. F., Bickle, M.J., Hawkesworth, C. J., Martin, A., Nisbet, E.G. and Orpen, J.C.

(1978). Granite greenstone terrains of the Rhodesian Craton. *Nature*. Vol. 27, pp. 23-27.

_____oOo_____